Numerical Verication of the Convexication Method for A Frequency-Dependent Inverse Scattering Problem with Experimental Data

Thuy Le,^{1,2,*} Vo Anh Khoa,^{3,**} Michael Victor Klibanov,^{1,***} Loc Hoang Nguyen,^{1,****} Grant W. Bidney,^{4,*****} and Vasily N. Astratov^{4,******}

¹Department of Mathematics and Statistics, University of North Carolina at Charlotte, Charlotte, NC 28223, USA

²Department of Mathematics, North Carolina State University, Raleigh, NC 27607, USA

³Department of Mathematics, Florida A&M University, Tallahassee, FL 32307, USA

⁴Department of Physics and Optical Science,

University of North Carolina at Charlotte, Charlotte, NC 28223, USA

The reconstruction of physical properties of a medium from boundary measurements, known as inverse scattering problems, presents signicant challenges. The present study aims to validate a newly developed convexication method for a 3D coecient inverse problem in the case of buried unknown objects in a sandbox, using experimental data collected by a microwave scattering facility at The University of North Carolina at Charlotte. Our study considers the formulation of a coupled quasilinear elliptic system based on multiple frequencies. The system can be solved by minimizing a weighted Tikhonov-like functional, which forms our convexication method. Theoretical results related to the convexication are also revisited in this work.

Keywords: Coecient inverse problem; gradient descent method; convexication; global convergence; experimental data; data propagation

1. INTRODUCTION

In this paper, we build upon our prior research and expand on the performance evaluation of our recently developed globally convergent convexication numerical method for solving a Coecient Inverse Problem (CIP) for the 3D Helmholtz equation using multiple frequencies. Our research aims to reconstruct the physical characteristics of explosive-like objects that are buried underground, including antipersonnel land mines and improvised explosive devices (IEDs). Thus, our focus is on three key properties: dielectric constants, locations, and the shapes of front surfaces.

One common approach for numerically solving a CIP is to minimize a conventional least squares cost functional, as described in previous literature such as [8, 11, 12]. However, this method has a major drawback-the cost functional is non-convex and often suers from the issue of multiple local minima and ravines. As a result, gradient-like methods are limited by getting stuck in any local minimum, and any convergence achieved is only guaranteed if the starting point is in close proximity to the correct solution. Therefore, conventional numerical methods for CIPs are generally limited to local convergence.

Denition. A numerical method for a CIP is referred to as globally convergent if there exists a theorem that guarantees the method will converge to at least one point within a suciently small neighborhood of the correct solution without requiring any prior knowledge of the neighborhood.

The convexication method is globally convergent, meaning that it is guaranteed to produce at least one solution within a suciently small neighborhood of the correct solution, without any prior knowledge of that neighborhood. This method is particularly well-suited for the most challenging cases of solving CIPs, whose data are both backscattering and non-overdetermined. In this context, data are considered non-overdetermined if the number m of free variables in the data is equal to the number n of free variables in the unknown coecient. In this paper, we consider the case where m = n = 3. It is worth noting that we are not aware of any other numerical methods for solving CIPs with non-overdetermined data at m = n + 2 that

^{*} Electronic address: tle55@uncc.edu,tle9@ncsu.edu

^{**} Electronic address: anhkhoa.vo@famu.edu,vakhoa.hcmus@gmail.com

^{****} Electronic address: mklibanv@uncc.edu
***** Electronic address: loc.nguyen@uncc.edu

^{******}Electronic address: gbidney@uncc.edu

^{*******}Electronic address: astratov@uncc.edu

are both based on the minimization of a conventional least squares cost functional and globally convergent according to the denition given above.

The convexication method has proven eective in solving a 3D CIP with a xed frequency and a point source moving along an interval of a straight line, as demonstrated by both computationally simulated [15] and experimental data [13, 14, 20]. In this scenario, we were able to accurately determine the rst two key criteria: the dielectric constants and locations of the experimental targets. However, imaging the shapes of the targets' front surfaces requires further improvements. For instance, when dealing with more complicated objects, as shown in Figures 6, 7, and 8, the previous conguration manifests several defects in the reconstructed images. Henceforth, the present paper is focused on further enhancing this aspect.

To address the limitations in imaging the targets' front surfaces with the existing method, we propose to use multiple frequencies while maintaining a xed point source for the CIP under consideration. This conguration has been previously studied in [24] in conjunction with the convexication technique to solve the same CIP using simulated data. However, its eectiveness with experimental data has only been demon-strated in producing good shapes of objects, while the reconstruction of the dielectric constant is not good. Therefore, we have no choice but to combine this conguration with the previous conguration, which uses a xed frequency and moving point sources, to amend the third property. In other words, we have gured out that the best would be to use a two-step procedure. Steps 1 and 2 are performed using two dierent versions of the convexication method. The version for Step 1 is described in this paper and the version for Step 3 was described in [1315].

Step 1. Use the backscattering data for a single location of the source and multiple frequencies. This gives us accurate geometrical characteristics of unknown targets: their locations and shapes of front surfaces. Especially complicated non-convex shapes with voids are imaged well, see images of letters U, A, O in Figures 68 below. However, values of dielectric constants of targets are not computed accurately on this step.

Step 2. Use the backscattering data for multiple locations of the source at a single frequency, as it was done in our previous papers [13, 14]. This provides us with accurate locations and accurate values of dielectric targets of targets, although the shapes of their front surfaces are not computed as accurately as they are in Step 1.

Step 3. Assign values of dielectric constants obtained on Step 2 to images obtained on Step 1. This completes our imaging procedure.

It is worth noting that the conguration of using multiple frequencies and a xed point source has been studied before in [26], but our approach in that study focused on a dierent approximation procedure using the tail function, rather than the convexication method explored in [24].

It should be noted that the proposed convexication approach for both the above-mentioned congura-tions builds upon the ideas of the BukhgeimKlibanov method. This method, which is based on Carleman estimates, was initially introduced in 1981 to establish proofs of uniqueness theorems for multidimensional CIPs, as detailed in the seminal work by Bukhgeim and Klibanov [7]. Since then, the method has been widely used and extended for solving various inverse problems, see e.g. [16] for a survey of this method.

The numerical approach considered in this paper deviates from other inversion techniques, such as those employed by Novikov's research group, as described in their publications [2, 3, 27]. These methods address single-frequency data and use distinct treatment methodologies. Additionally, we make reference to [4] for a diverse numerical approach to a similar CIP.

The structure of this paper is as follows. In section 2, we introduce the Coecient Inverse Problem (CIP) and the corresponding forward problem. Section 3 is devoted to the derivation of our functional J and the presentation of our theoretical results, which are based on our recent publication [24]. Then, our experimental ndings are provided in section 4. Finally, we close the paper by some concluding remarks in section 5.

2. STATEMENTS OF THE FORWARD AND INVERSE PROBLEM

While the Maxwell's equations are the primary governing equations for the propagation of electromagnetic waves, our paper employs the Helmholtz equation. This approach is supported by numerical demonstrations presented in the appendix of the paper [28], which establish that the Helmholtz equation eectively characterizes the propagation of a specic component of the electric eld. Additionally, our successful experimental ndings, as reported in our recent publications [2,3], provide further validation for the use of the Helmholtz equation in this context.

Let be the Dirac function. Consider the following time-harmonic Helmholtz wave equation with $x = (x; y; z) 2 R^3$.

$$u + !^{2} (x) u = (x x)$$
 in R^3 ; $i = \frac{p}{1}$: (1)

Physically, u = u(x) can be interpreted as a component of the electric eld $E = (E_x; E_y; E_z)$ that corresponds to the non-zero component of the incident eld. Specically, in our case, the incident eld is characterized by the voltage E. In our experiments, we measure the backscattering signal of this same component. Additionally, ! represents the angular frequency in rad/m, while and "0 (x) denote the permeability (H/m) and permittivity (F/m) of the medium, respectively. The point source x is xed in this study.

We restrict our settings to non-magnetic targets, which means that the materials under consideration have no magnetic properties, and therefore their relative permeability is equal to one. To be more precise, this implies that the ratio of the permeability of the material to the permeability of free space (i.e., vacuum) is unity. Let " $_0$ represent the vacuum permittivity and let $_0$ denote the vacuum permeability. Consider k = 0" $_0$, equation (1) can be rewritten as

$$u + k^2 \frac{{}^{"0}(x)}{{}^{0}_{0}} = (x - x)$$
 in R^3 : (2)

We can now express the spatially distributed dielectric constant as $c(x) = "^0(x) = "_0$. Using this, the conventional Helmholtz equation follows from (2) and applying the Sommerfeld radiation condition, we get the following system.

$$u + k^2 c(x)u = (x x) \text{ in } R^3;$$
 (3) $\lim_{r \mid 1} r(@_r u \text{ iku}) = 0 \text{ for } r = jx \text{ xj}; i = p_{\underline{-1}}$: (4)

Let us now focus on a rectangular prism , dened as (R;R) (B;b) in B^3 for B;b>0. This prism serves as our computation domain of interest. Besides, we dene the lower side of the prism as the near-eld measurement site,

$$:= fx : jxj; jyj < R; z = bg:$$

In what follows, we make the assumption that the dielectric constant is smooth and meets the following conditions:

(
$$c(x) 1 in$$
 ; (5) $c(x) = 1 in R^3 n$.

The second equation in (5) indicates our assumption that the region outside of the domain is a vacuum. Next, we consider the line of sources that is parallel to the x-axis and exists outside of the closure

. Mathematically, the following line of sources, denoted as L_{src}, is examined:

$$L_{src} := f(; 0; d) : a_1 \ a_2g;$$
 (6)

where d > b and $a_1 < a_2$. Note in this setting that the distance between the line of sources L_{src} and the xy-plane is d. With this conguration in place, we can now select and describe the xed point source. The value of R; d; b; a_1 ; a_2 ; will be specied in our experimental results.

Remark 1. To this end, we dene the total wave u_i , incident wave u_i , and scattered wave u_s . It is worth noting that $u = u_i + u_s$. Besides, the Sommerfeld radiation condition (4) is applied to guarantee the existence and uniqueness results for the Helmholtz equation (3); cf. [9, Chapter 8].

Remark 2. In our conguration of interest, we arrange to measure the data with multiple frequencies. In this regard, the involved waves $u; u_i; u_s$ are dependent of k. Henceforth, in the sequel, we write $u = u(x; k); u_i = u_i(x; k); u_s = u_s(x; k)$ for $k \ge [\underline{k}; \overline{k}]$, where $\underline{k}; \overline{k} > 0$.

2.1. Forward problem

Prior to introducing the forward problem, we model the incident wave by using the point source,

$$u_i\left(x;k\right) = \frac{exp\left(ik\,jx\,-\,xj\right)}{4\,jx\,-\,x\,-\,j}. \tag{7}$$
 We observe that the incident wave u_i satises the Helmholtz equation in the form of (4) with $c(x)$ = 1. By

We observe that the incident wave u_i satises the Helmholtz equation in the form of (4) with c(x) = 1. By subtracting (4) from the Helmholtz equation for u_i , we can obtain the PDE for the scattered wave u_s as follows.

$$u_s + k^2 u_s = k^2 (c(x) 1) u$$
:

Cf. [9], the scattered wave is solved via the following integral equation:

$$u_{s}(x;k) = k^{2} \frac{Z_{exp}(ik jx - x^{0}j)}{4 jx - x j^{c}} (c(x^{0}) - 1) u(x^{0};k) dx^{0}$$

$$= k^{2} \frac{exp(ik jx - x^{0}j)}{4 jx - x j^{c}} (c(x^{0}) - 1) u(x^{0};k) dx^{0}; \quad x \geq R^{3};$$
(8)

where we have used the fact that c 1 is compactly supported in

; see (5). Combining (7) and (8), we arrive at the so-called Lippmann-Schwinger equation:

$$u(x;k) = u_i(x;k) + k^2 \frac{Z}{4 |x - x^0|} \frac{\exp(ik jx - x^0 j)}{4 |x - x^0|} (c(x^0) - 1) u(x^0;k) dx^0; \quad x \ge R^3$$

Hence, our forward problem is to determine the boundary information of the total wave eld u(x;k)j for $k \ 2 \ \underline{[k;k]}$, based on the known dielectric constant c. It is important to remark that the total wave eld can be non-zero for all points x in the domain and for large values of k, as demonstrated in [15, 24] when c belongs to $C^{15}(R^3)$ and the Riemannian geodesic line connecting x and x is unique.

2.2. Coecient inverse problem (CIP)

Our CIP is to seek the dielectric constant c(x) satisfying (5) from knowledge of the boundary measurement $F_0(x;k)$ of the near-eld data,

$$F_0(x; k) = u(x; k)$$
 for x 2; k 2 [k; \overline{k}]; (9)

where u(x; k) is the total wave associated with the incident wave $u_i(x; k)$ in (7).

While a more detailed description of our experimental setup will be provided in the numerical section, we would like to provide a brief overview. In order to simulate the detection of land mines buried underground, we have buried a single inclusion in a sandbox, with the sand understood as our background medium. The dielectric constant of the sand, c_{bckgr} , is known a priori to be about 4. Although we do not utilize this information in our numerical method, the inclusions in our resulting images are characterized by a dielectric constant c(x) greater than this number 4. It is important to note that the function c(x) used in our mathematical statements incorporates information from both the sand and the inclusion. In order to address this, we measure the raw data twice in our conguration: once when the sandbox is empty, and again when the target is buried within it. By subtracting the former from the latter, we can lter out the information related to the sand. The resulting actual data (i.e., after subtraction) can then be used in the mathematical setting under consideration.

Our choice to use near-eld data stems from our experimental observations, which have shown that far-eld data alone do not provide an accurate indication of the buried object's location. In contrast, near-eld data have been found to be more reliable, as reported in [13, 14, 26] and numerically observed in Figure 3. Furthermore, using near-eld data allows us to reduce the size of the computational domain, thereby increasing accuracy, since the number of mesh grids is xed in our experiments.

Experimentally, we cannot get the near-eld data, but the far-eld. The near-eld we mean is the approximate dataset that is calculated from the experimental far-eld data. To obtain the near-eld data, we employ a technique known as data propagation; cf. [13, 26], the technique is revisited in section 4.

This procedure involves eliminating high spatial frequencies to obtain a good approximation of the near-eld function F_0 in (9). While we only obtain the measured data F_0 , our mathematical model requires the z derivative of the function $u\left(x;k\right)$ on f_0 ,

$$F_1(x; k) = @_z u(x; k) \text{ for } x \ 2 \ ; k \ 2 \ \underline{[k; k]}$$
: (10)

Remark 3. Given the CIP above, our data are non-overdetermined since the number m of free variables in the data equals to the number n of free variables in the sought coecient. In particular, m = n = 3 in this scenario.

Remark 4. In the context of multiple sources and a xed frequency, as presented in e.g. [15], our CIP can be expressed in a similar way. Specically, we can consider as the source variable based on the denition of the line of sources in (6). To handle the conguration of multiple sources and a xed frequency, we require the boundary measurement $F_0(x;)$, which corresponds to F_0 in (9), and the Neumann-type measurement $F_1(x;)$, which corresponds to F_1 in (10). Thereby, to derive a coupled quasi-linear elliptic system and establish the convexication, as discussed in section 3, we can replace the frequency variable k with the source argument in our formulations. The reader can be referred to Figure 1 for a visual representation showing the dierence in the setup between the two distinct congurations.

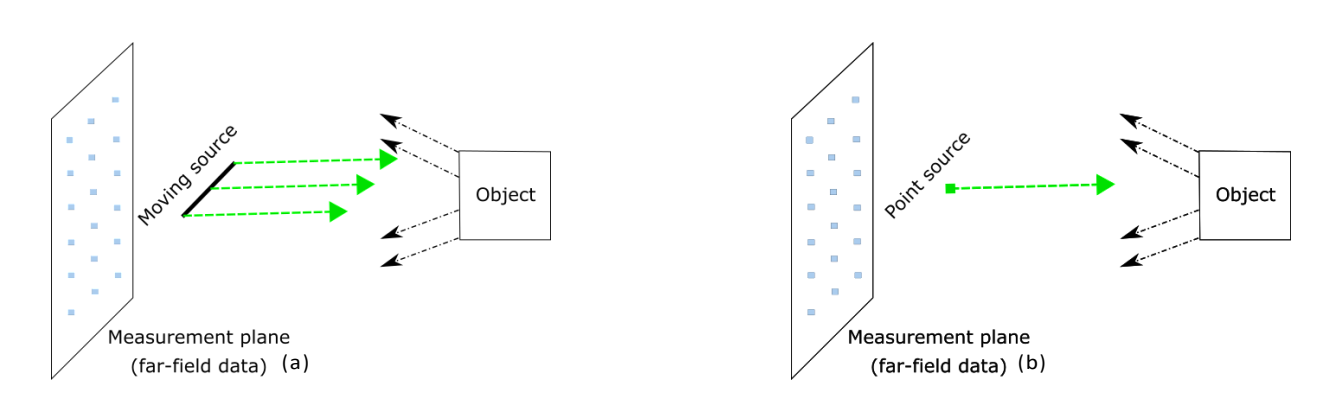


FIG. 1. (a) Conguration that involves the utilization of multiple sources arranged along a straight line. Each source emits an incident wave at a xed frequency. (b) Conguration that uses a xed source while varying the frequency of the generated signal. For both distinct congurations, there are detectors on the measurement plane to collect the backscattering data.

3. CONVEXIFICATION

3.1. Derivation of a coupled quasi-linear elliptic system

For x 2
$$\frac{1}{and \ k \ 2 \ [k;k]}, \ we \ dene \ v \ (x;k) = \ _{k^2} \ log \ _{u_i (x;k)} \ . \ lt$$

$$r \ v \ (x;k) = \ _{follows \ from \ simple \ calculations \ that \ 1 \ ru \ (x;k) \ } ru_i \ (11)$$

$$(x;k) \ _{k^2} \ u \ (x;k) \ u_i \ (x;k)$$

$$v \ (x;k) = \ _{u_i (x;k)} \frac{1}{u \ (x;k)} \frac{u_i \ (x;k)}{u \ (x;k)} + \frac{r \ u_i \ (x;k)^2}{u_i \ (x;k)} \frac{\#}{k^2} \ : \ (12)$$

When x , we know that the total wave eld u(x;k) satises the homogeneous Helmholtz equation, $u+k^2c(x)u=0$. The incident wave $u_i(x;k)$ also satises this Helmholtz equation with c(x)=1. In other words, it holds true that

$$\overline{u_i(x;k)} = k^2 c(x); \qquad \overline{u_i(x;k)} = k_2: u_i(x;k)$$

Combining this with (11), (12), we obtain the following nonlinear PDE for the function v = v(x; k):

$$v + k^{2}(rv)^{2} + \frac{2rv ru_{i}}{u_{i}} = c(x) + 1$$
 (13)

for all x 2

and k 2 [k; k]. By dierentiating (13) with respect to the argument k, we arrive at the following nonlinear

$$@_{k}v + 2k^{2}rv \ r@_{k}v + 2k(rv)^{2} + 2r@_{k}v \ \stackrel{ru_{i}}{\underset{i}{\leftarrow}} + 2rv@_{k} \ \stackrel{ru_{i}}{\underset{i}{\leftarrow}} = 0:$$
(14)

At this stage, it is worth noting that the PDE (14) does not contain the unknown function c(x), which is the quantity of interest in our CIP. By solving PDE (14), we can obtain the dielectric constant c(x) via the backsubstitution in PDE (13).

We, on the other hand, obverse that Equation (14) is a non-trivial third-order PDE. Therefore, we rely on the use of a special orthonormal basis of $L^2(\underline{k}; k)$. Denoted by f ${}_mg_{m1}$, this basis is rst established in [17], and it has been applied to solve distinctive inverse problems for PDEs with direct applications to, e.g., electrical impedance tomography and imaging of land mines our target application in this work. The reader can be referred to [13, 19, 21] and references cited therein for an overview of such inverse problems.

To construct this basis, for each m 1 we consider $m(k) = k^{m-1}e^{k-(k+k)}=2$. The set $f'_m(k)g_{m1}$ is lin-early independent and complete in L^2 \underline{k} ; k. We then apply the standard Gram-Schmidt orthonormalization procedure to obtain the basis $f_m(k)g_{m1}$.

- The basis f $_{m}$ (k)g $_{m1}$ has the following properties: $_{m}$ 2 C 1 \underline{k} ; k_and 0 is not identically zero for any m 1;
 - ^ Let $S_{mn} = h^{-0}$; mi Where h; i denotes the scalar product in L^2 \underline{k} ; k... Then the square matrix $S_N = (S_{mn})_{N : n=1}^n 2 R^{NN}$ is invertible for any N since

$$S_{mn} = \begin{cases} 1 & \text{if } n = m; \\ 0 & \text{if } n < m; \end{cases}$$

Notice that the second property does not hold for either classical orthogonal polynomials or the classical basis of trigonometric functions. The rst column of S_N obtained from either of the two conventional bases

To solve the third-order nonlinear PDE (14), we consider the truncated Fourier series using the abovementioned basis. In particular, for x 2

and k 2 k; k, we seek

$$v(x;k)$$
 $v_n(x)$ $v_n(x)$ $v(x;k)$ v

By plugging (15) into the third-order PDE (14), we nd that

$$X^{N} v_{n}(x) = \sum_{n=1}^{N} rv_{n}(x) rv_{m}(x) k^{2} v_{n}(k) + k v_{n}(k) v_{m}(k) v_{n}(k) + k v_{n}(k) v_{m}(k) v_{m}(k) v_{n}(k) v_{$$

Henceforth, for 1 | N we multiply both sides of (16) by I(k) and obtain the following PDE system:

$$X^{N} = X = X = N = 1$$

$$S_{In}v_{n}(x) + P_{Inm}rv_{n}(x) rv_{m}(x) + Q_{In}(x) rv_{n}(x) = 0:$$

$$S_{In}v_{n}(x) + R_{Inm}rv_{n}(x) rv_{m}(x) + R_{Inm}rv_{n}(x) rv_{m}(x) = 0:$$

$$S_{In}v_{n}(x) + R_{Inm}rv_{n}(x) rv_{m}(x) + R_{Inm}rv_{n}(x) rv_{m}(x) + R_{Inm}rv_{n}(x) rv_{m}(x) + R_{Inm}rv_{m}(x) rv_{m}(x) + R_{Inm}rv_{m}(x) rv_{m}(x) + R_{Inm}rv_{m}(x) rv_{m}(x) + R_{Inm}rv_{m}(x) rv_{m}(x) rv_{m}(x)$$

In (17), we have for m; n; $l = \overline{1; N}$ that

$$\begin{split} S_{In} &= \sum_{n=0}^{\infty} (k) _{n}(k) _{k}(k) dk; \\ &= \sum_{k=0}^{\infty} \frac{k^{2} _{n}(k) _{m}(k) + k _{n}(k) _{m}(k) _{k}(k) dk; \\ Q_{In}(x) &= 2 \sum_{k=0}^{\infty} (k) _{u_{i}(x;k)}^{r u_{i}(x;k)} _{u_{i}(x;k)} (k) @_{k} _{u_{i}(x;k)}^{r u_{i}(x;k)} (k) dk; \end{split}$$

Now recall from (9) that we measure the wave u on the lower side $\,$ of the prism . Therefore, the Dirichlet boundary information of the sought Fourier coecients $v_n(x)$ for 1 n N is given by

$$g_{0n}(x) = \sum_{k}^{Z_{\overline{k}}} k^{2} \log [F_{0}(x; k) = u_{i}(x; k)] \quad _{n}(k) dk \quad \text{for } x \ 2 :$$
 (18)

$$g_{0n}(x) = 0$$
 for x 2 @ (19)

As mentioned in the previous section, the Dirichlet measured data (9) can lead to the Neumann-type data (10). Moreover, we can compute that for $x \ 2$

Henceforth, the Neumann-type boundary information of the source Fourier coecients $v_n(x)$ for 1 $\,$ n $\,$ N is given by

g (x) =
$$Z_k k^2 \frac{1}{F_1(x;k)} \frac{1}{Q_2 u_i(x;k)}$$

 $E_1(x;k) = \frac{1}{Q_2 u_i(x;k)} \frac{1}{Q_3 u_i(x;k)} \frac{1}$

Associating (17) with (18), (19), (20) forms our system of coupled elliptic equations, whose solution is the vector function V(x) that contains all all of the Fourier coecients v_n for $1 \, n \, N$.

3.2. Convexied costs functional and theorems revisited

It is evident that (17) is a system of coupled quasi-linear elliptic equations. The nonlinear terms are generated by products of gradients $rv_n(x)rv_m(x)$. Therefore, conventional least-squares methods, which minimize the dierential functional, may not yield desirable results. Nonlinear problems often exhibit nonconvex cost functionals, resulting in multiple local minima and ravines. Hence, a good initial guess must be chosen to reach the global minimizer.

To tackle nonlinear inverse problems, convexication is one of some numerical methods available. This method and its variants construct a suitable weighted cost functional that is strongly convex over a bounded set of a Hilbert space. With this approach, the existence and uniqueness of a minimizer can be proven without any restriction on the size of the set. Additionally, convergence towards the correct solution is guaranteed.

Introduce = $(z) = e^{-(R+r)^2} e^{(z-r)^2}$ as the Carleman Weight Function (CWF). Then, we consider the following weighted cost functional J:[H (p-N)] R_+ , for p>3,

Here, the CWF plays several important roles in the convexication of interest. First, the function helps to control the highly nonlinear terms in the target quasi-linear system. Second, the CWF appears to maximize the inuence of the measured boundary data at . Lastly, by the presence of such a function, one can prove that the cost functional is globally strongly convex.

From now onward, we state the minimization problem.

Minimization problem. Minimize the cost functional J(V) on the set $\overline{B(M)}$,

n o B (M) = V 2 [H^p(N)] :
$$kV k_{[H^p()]}$$

Now, we formulate theorems of our convergence results. The theorems were proven in, e.g., [15, 24]. Therefore, their proofs are omitted. We begin with the Carleman estimate for the continuous Laplacian.

The next theorem is devoted to the global strong convexity of the cost functional J(V).

Theorem 2. The functional J (V) dened in (21) has its FrØchet derivative D J for all V 2 $B(\overline{M})$. Moreover, we can \underline{nd} a suciently large = (M;) > 0 such that $\overline{J(V)}$ is strongly convex on B(M). In particular, for all V₂; V₁ 2 B(M), we have

where C = C(M;) > 0.

As a by-product of Theorem 2, the existence and uniqueness of a minimizer V_{min} in $\overline{B(M)}$ are guaranteed. Moreover, we obtain the Lipschitz continuity of the FrØchet derivative D J on $\overline{B(M)}$; see e.g. [15, Theorem 5.2] and some other references cited therein.

The convergence result follows from [29, Theorem 6]. Following the Tikhonov regularization concept [6], we assume the existence of the exact solution V 2 [H p ()] N of System (17) and that it satises the noiseless data g and g . Here, g and g are, respectively, corresponding to the noisy boundary data g_0 and g_1 , whose elements are dened in (18), (19), (20).

Let > 0 be the noise level. We assume that there exists an error function E 2 [Hp(

Next, we assume the existence of a function V such that @V = g_0 on @ and V = g_1 on . Consider $V_{min;"}$; $(x) = V_{min}(x) + V(x)$ for x 2 . The convergence theorem is stated in the following.

Theorem 3. Assume that

Then we can nd a constant C = C (

; r; M) such that the following estimate holds true $kV_{min;";}$ $Vk_{\left[H^{2}\right(}$ $p_{...}$

$$(B_{11N} + C_{11N} + C_{$$

Since smallness conditions are not imposed on M, then the above convergence estimate conrms the global convergence of the minimizer of the cost functional J(V) to the exact solution.

It now remains to discuss how to nd $V_{min;"}$; by the so-called gradient descent method. Let 2 (0;1). The gradient descent method is given as follows:

$$V^{(n)} = V^{(n-1)} DJ(V^{(n-1)}); n = 1; 2; ...;$$
 (22)

where V $^{(n)}$ denotes the nth iteration for the approximation of the minimizer $V_{min;"}$;. In (22), we use the starting point V $^{(0)}$ 2 B(M) being an arbitrary point in that particular set. Recall that by Theorem 2, we obtain that $V_{min;"}$; in B(M). Cf. [25, Theorem 2], if we assume further that the ball centered at $V_{min;"}$; with the radius V $^{(0)}$ $V_{min;"}$; $V_{min;"}$

 $_{)]^{N}}$ is contained in B(M), then the distance between the nth iteration $V^{(n)}$ and the minimizer $V_{min;";}$ is controlled well by that radius $V^{(0)} = V_{min;";}$ [H²()] $_{]1^{N}}$. In particular, we formulate the following theorem, while its proof is omitted.

Theorem 4. Let $V^{(0)}$ 2 B (M) and $V_{min;";}$ 2 B (M) be such that the ball centered at $V_{min;";}$ with the radius $V^{(0)}$ $V_{min;";}$ $V_{min;";}$

is contained in B(M). Then there exists a suciently small number $_0$ 2 (0;1) such that $V^{(n)}$ B (M) for all n=1;2;::: and for all 2 (0; $_0$). Moreover, there exists a number &= &() 2 (0;1) such that

$$V^{(n)} V_{min;"};_{[H^2(V_{min};"];_{[H^2(V_{$$

By Theorems 3 and 4, we obtain the strong convergence of the sequence $fV^n g_{n=0}^1$ toward the exact solution V. Particularly, by the triangle inequality, it holds true that

y, by the triangle inequality, it holds true that
$$V^{(n)} \ V \ C^{p} \ kV \ Vk \ H^{p(n)} \ + + \&^nV^{(n)} \ V \ H^{2(n)} \ H^{2($$

4. NUMERICAL EXPERIMENTS

The numerical results performed in this section are all obtained with experimental data. Those are data collected at the microwave facility of the University of North Carolina at Charlotte (UNCC), USA. For the sake of simplicity, we refer the reader to [13, 14] for details of the experimental setup we establish at the University of North Carolina at Charlotte. Thereby, we only mention below key elements of our experimental conguration. Even though those publications [13, 14] focus wholly on the CIP with multiple point sources and a xed frequency, the set of data collected at that time is variable in both source locations and frequencies for trial-and-error. For each source position, our raw data set consists of back-scattering data corresponding to 201 frequency values uniformly distributed between 1 GHz to 10 GHz. Therefore, we are capable of using those data to verify the numerical performance of the convexication method for the CIP in the context of multiple frequencies and a xed point source.

4.1. Experimental conguration and computational settings

The experiment conducted at UNCC involves practical data of ve (5) experimental objects buried in a sandbox. Those tested objects were prepared to mimic explosive-like devices often seen in the battleeld. Typically, we classify them as metallic and non-metallic objects:

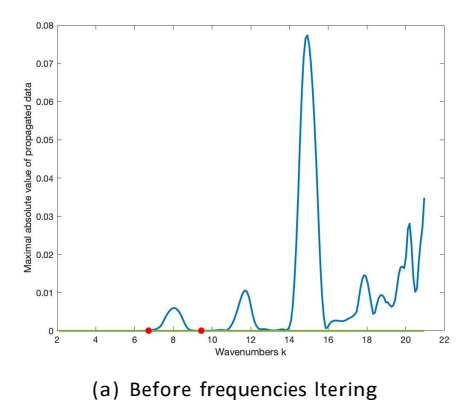
- 1. An aluminum tube that mimics the NO-MZ 2B, a Vietnamese anti-personnel fragmentation mine; cf. [5].
- 2. A glass bottle lled with clear water that is a good t of the Glassmine 43 in terms of the material; cf. [28]. Reconstructing the shape of the bottle is challenging as this object comes with a cap.
- 3. An U-shaped piece of a dry wood that can be an example of the Schu-mine 42, a wood-based anti-personnel blast mine. Compared to the glass bottle above, this piece of dry wood has a very complicated non-convex shape.
- 4. A metallic letter 'A' that is to augment the complication in shape of metallic experimental object; compared to the aluminum cylinder.
- 5. A metallic letter 'O' that serves the same purpose as the letter 'A'. It helps to test the numerical performance of the convexication method with varying levels of complexity in the shape of the object.

In [13], the last two tests (i.e. those with the metallic letters) were blinded. In this sense, we only knew their backscattering data and that the experimental objects were buried close to the sand surface. The experimental results obtained in that publication, however, turn the blinded tests to be unblinded. Therefore, in the present paper, our numerical experiments are demonstrated with all unblinded tests.

For every test, the experimental object is placed inside of a rectangular box lled with moisture-free sand, which is then referred to as a sandbox. This man-made sandbox is framed by some wood materials, and its back and front sides are covered by a 5-cm layer of Styrofoam. The front side we mean here is closer to the standard antenna, compared to the back one. In our conguration, the antenna plays a role in sending incident waves toward the sandbox. Then, there is a rectangular measurement surface of dimensions 100100 (cm²) behind the antenna to collect the backscattering data. Experimentally, this surface is discretized in an equidistant mesh of 2-cm mesh-width. Moreover, the horizontal and vertical sides of this surface dene, respectively, the x- and y-axes of our coordinate system and thus, the z-axis is the orthogonal one to our measurement plane. As to the burial depth of the experimental object, it is a few centimeters away from the front Styrofoam. This is relevant to real-world applications that landmines are at most 10 (cm) away from the ground surface in the battleeld; cf. [10].

In the sequel, we consider dimensionless variables as $x^0 = x = (10 \text{ cm})$ and for simplicity, we use the same notations as in the theoretical part. In this regard, the dimensions in our computations are 10 times less than the real ones in centimeters. For instance, our 100 100 (cm²) measurement plane is understood as a 10 10 surface in the dimensionless regime. Now, we introduce our computational setup in this dimensionless setting. According to our experiment, the distance between the measurement surface and the sandbox with the front Styrofoam is 11.05. We also nd that the length in the z direction of our sandbox without the Styrofoam is about 4.4. As the Styrofoam layer is bent by the intensity of dry sand, we deliberately reduce 10% of this result choice length. of these in the of our computational $= x 2 R^3$: jxj; jyj < 5; jzj < 2. In other words, we take R = 5, b = 2, and the center of the sandbox is taken as the origin of our coordinate system. As to the source position, in our numerical results below we choose the one adjacent right to the origin of the line of sources in [13, 14]. The location of this source is (0:1; 0; 9).

Our raw data are measured far away from the sandbox. Cf. [13, 14, 26], we observed numerically that these data lack quality due to many physical diculties met in measurement process (antenna location, unwanted furniture with dierent materials, distracting signals). It will be then not good if we apply them directly to the minimization procedure. Thus, we employ the so-called data propagation technique to move these far-eld data closer to the sandbox, which results in an approximation of the near-eld data. It is also worth mentioning that the application of this data propagation procedure is helpful in reducing the size of the computational domain in the z-direction. Thus, it gives a better estimation of images of the experimental objects in x; y coordinates. In this work, the near-eld plane is chosen as $x \in \mathbb{R}^3$ is $x \in \mathbb{R}^3$.



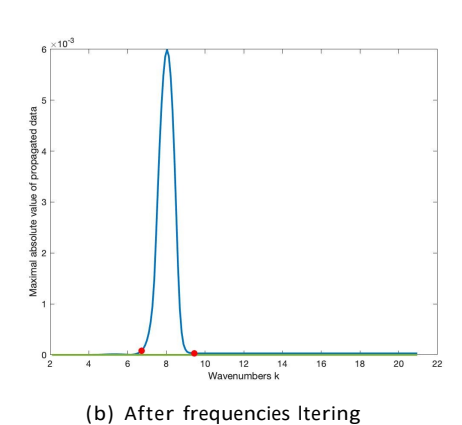
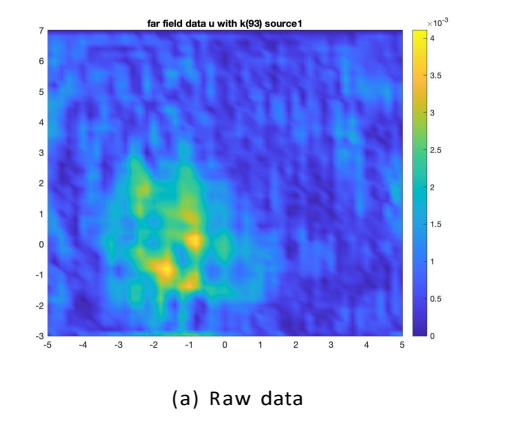


FIG. 2. Illustration of the frequencies ltering for preprocessed data in Example 1. (a) The frequency dependent dynamics of the maximal absolute values of the experimental data after preprocessing procedure. All of these values are depicted for all wavenumbers k 2 [2:09; 20:95] corresponding to the frequencies f´ 2 [1 GHz; 10 GHz]. The red dots are imposed to indicate the wavenumber interval should be chosen. (b) The maximal absolute values of the processed data after frequencies ltering.

We revisit the data propagation procedure that enables us to obtain the propagated data, termed as near-eld data, from the raw data referred to as far-eld data. We know that c(x) = 1 outside of the rectangular



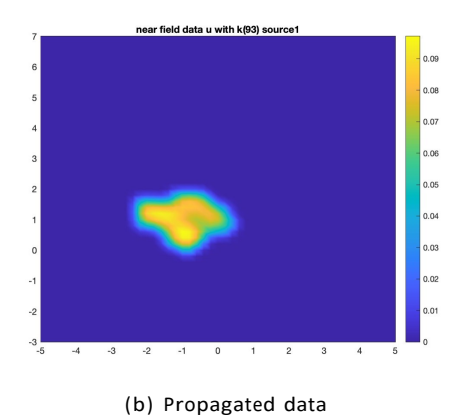


FIG. 3. Graphical illustration of the absolute value of the raw far-eld data (a) and the propagated near-eld data (b) in Example 4 in which the experimental object is A-shaped. This set of data is collected at k = 10:77 corresponding to f~= 5:14 (GHz), see (26) for the relation between the wavenumber k and the frequency f. From these gures, we can see the A shape very clear when using the propagated near-eld data. Meanwhile, the shape is not captured well for the raw far-eld data.

Example	1	2	3	4	5
Object	Metallic cylinder	Bottle of water	Wood U	Лetallic A Ме	tallic O
Wavenumber k	6.72 - 9.45	5.87 - 8.60	18.22 - 20.96	10.68 - 13.41	8.70 - 11.43
Frequency (GHz)	3.21 - 4.51	2.80 - 4.11	8.70 - 10	5.10 - 6.40	4.15 - 5.46

TABLE 1. The case of a single location of the source and multiple frequencies. Distinctive choices of the wavenumber interval for examples 1-5 and the corresponding frequencies.

prism

= (R;R)(R;R) (b;b) in R^3 . Therefore, the scattered wave u_s in the half space fz < g bg satisfs the following system:

$$u_s + k^2 u_s = 0$$
 in fz < bg; (23)

$$u_s + k^2 u_s = 0$$
 in fz < bg; (23)
 $\lim_{r \mid 1} r(@_r u_s \quad iku_s) = 0$ for $r = jx \quad xj$; $i = p$ —1: (24)

As mentioned in section 2, our experiments make use of the far-eld data. Consequently, we have a dataset denoted as $u_s(x; y; D)$, where D > b, while our objective of the data propagation procedure is to obtain $u_s(x; y; b)$. Specically, in our experiments, we have D = 14. The data propagation is obtained in the following way. Consider the Fourier transform of the scattered wave:

F
$$(u_s)(1;2;z) = \frac{1}{2^{R^2}} u_s(x) e^{-i(x_1+y_2)} dxdy;$$

assuming that the corresponding integral is convergent. For z < b, by applying the same Fourier transform to equation (23), we nd that

$$@_{2zz}F(u_s) + k^2 {}^2 {}_2F_2(u_s) = 0:$$

Solving the above dierential equation gives the following relation between $F(u_s)(z)$ at $z < \infty$

Example	1	2	3	4	5
Object	Metallic cylinder	Bottle of water	Wood U N	letallic A Me	tallic O
Wavenumber k	8.51	6.62	11.43	9.55	8.79
Frequency (GHz)	4.06	3.16	5.45	4.55	4.19

TABLE 2. The case of a single frequency and multiple sources. Distinctive choices of the wavenumber for examples 1-5 and the corresponding frequencies.

$$F(u_s)(z = b),$$

$$F(u_s)(z) = \begin{cases} (u_s)_p (\frac{p_{\frac{2+2-2}{1}}}{b^2} \frac{p_{\frac{2+2-2}{2}}}{b^2} \frac{p_{\frac{2+2-2}{2}}}{b^2} \frac{p_{\frac{2+2-2}{2}}}{b^2} \frac{for^2 + 2 k^2}{b^2} \\ c_1 e^{-i} \frac{p_{\frac{2+2-2}{2}}}{b^2} \frac{p_{\frac{2+2-2}{2}}}{b^2} \frac{for^2 + 2 k^2}{b^2} \end{cases}$$
 otherwise:

Cf. [26, Theorem 4.1], we can set $C_2 = 0$ in (25). For D relatively large, the value of the term in the rst line of (25) is very small. Therefore, we can neglect the term with high frequencies and then use the inverse Fourier transform to obtain the near-eld data:

$$u_{s}(x;y;b) = \frac{1}{(2)^{\frac{2}{2}}} F(u_{s})(_{1};_{2};D) e^{i h p_{k^{2} - 2}} e^{i (D+b)+x_{1}+y_{2}} d_{1}d_{2}:_{2}+2 < k^{2}$$

As an slight improvement of the data propagation technique commenced in [26], we postulated a modied truncation procedure in [13] to remove possible random oscillations in the propagated data. The truncation procedure consists of two steps. First, we only preserve the propagated data whose values are at least 40 percents of the maximum absolute value. Then, we smooth those truncated data by the Gaussian Iter. Observe that the smoothing process will average out the maximum value of the data, which may impact on the accuracy of the minimization result. In the second step, we add back some percents of the smoothed data to preserve the important peak that represents the maximum absolute value of the data. When doing so, we only need to multiply the smoothed data by a retrieval number computed by max (jtruncated dataj) = max (jsmoothed dataj). This whole notion is mathematically specied in [13], and the reader should be referred to that publication for any other details.

We now discuss the choice of an appropriate frequency interval since it does aect the quality of the frequency-dependent data applied to the minimization process. We remark that the raw data are frequency dependent in which the frequency unit is Hz (or s ¹). Cf. [13, 26], we formulate the relation (in the dimensionless regime) between the wavenumber k (with unit cm ¹) and the frequency, denoted by f, as follows:

$$2f^{\sim}$$
 (26) k = 2997924580:

The choice of a frequency interval essentially relies on the performance of the data after preprocessing. Experimentally, it is dierent from one example to the others; see Table 1. Following two criteria proposed in [26], we choose the wavenumber interval such that (1) the maximal absolute value of the processed data in this interval should not soar and plunge dramatically, and (2) for distinctive frequencies within this interval, these maxima at attained at the same coordinates (small deviation is acceptable) of the near-eld plane. Once the interval is determined, we truncate all data that are outside of the chosen interval. Presenting the maximal absolute values of the experimental data in Example 1 after preprocessing for all wavenumbers k, Figure 2 exemplies well the above-mentioned strategy. We nd numerically that in Example 1, the interval of wavenumbers should be the vicinity of the rst bump with a length of about 2.7 (see red dots in Figures 2(a) and 2(b)). Note that since our frequencies f are between GHz and 10 GHz, the corresponding wavenumber k should range approximately from 2.09 to 20.95 using (26). We apply the same process to all other examples to choose appropriate wavenumber intervals for them. Tentatively, we call this process frequencies ltering.

4.2. Minimization process

Theoretically, our convexication method is globally convergent for any initial solution V $_{0}B$. However, to reduce the elapsed time of computations, we deliberately nd the initial solution $V_{0} = v_{1}^{(0)}; \dots; v_{N}^{(0)}$ that is close to V. Recall that $V = (v_{1}; v_{2}; \dots; v_{N})^{T}$ is the solution of the following nonlinear elliptic system:

associated with the boundary conditions @Vj = g₀; V j_@

= g_1 . Note that g_0 and g_1 are obtained from our experimental data after the frequencies Itering process. In (27), we indicate that for i; j; l = 1; N,

$$S_{In} = \sum_{k=0}^{K} f(k) = f(k) = f(k) dk;$$

$$\sum_{k=0}^{K} Z_{k}$$

$$P_{Inm} = 2 \sum_{k=0}^{K} k^{2} = f(k) \sum_{m=0}^{0} f(k) + k = f(k) = f(k) dk;$$

$$Q_{In}(x) = 2 \sum_{k=0}^{K} f(k) \frac{ru_{i}(x;k)}{u_{i}(x;k)} + f_{i}(k)@_{k} \frac{ru_{i}(x;k)}{u_{i}(x;k)} = f(k)dk;$$

where the upper and lower bounds of k are determined in the frequencies Itering mentioned above.

It is thus natural to take V_0 solutions to the corresponding linear system to (27). In this sense, we drop in (27) the nonlinear term containing rv_n (x) rv_m (x) and therefore, arrive at the following linear elliptic system:

$$X^{N}$$
 $S_{ln}v_{n}(x) + X^{N}$ $Q_{ln}(x) rv_{n}(x) = 0$ for all $l = 1; \overline{N}$ (28)

associated with the same boundary conditions g_0 and g_1 . By the natural linearity, system (28) can be solved directly by the quasi-reversibility (QR) method involving the same Carleman weight function = $(z) = e^{(R+r)^2}e^{(z-r)^2}$. In this regard, we minimize the following functional:

The solution V_0 obtained from solving (28) will be used as the starting point of the minimization process. Implementation of this QR method in a nite dierence setting is detailed in [24, 25] and is analogous to the implementation of our cost functional J (V) below.

As introduced in section 3, the cost functional of our minimization process for system (27) is formulated as follows:

Here, recall that $= (z) = e^{-(R+r)^2} e^{(z-r)^2}$ involves the Carleman weight function $e^{(z-r)^2}$. In our numerical verication, we choose = 1:1 and r = 5:5 in (31). We remark that even though our theory is valid for suciently large values of , we have experienced numerically that we can choose a moderate value of in [1,3]; see our previous works with both simulated and experimental data [1315, 18]. Below, we use the same value of " $= 10^9$ for all examples. Also, instead of using a high regularity in the regularization term "kV k $_p$ $_N$, we use only "kV k $_{2N}$. It reduces the computational complexity, while still providing a satisfactory numerical performance. As in [13], the cut-o number for our Fourier series is chosen as N = 6 in all examples. Besides, the same parameters are used in our minimization of the quadratic functional (29) of the QR method in all tests.

We now briey mention the standard fully discrete version of the cost functional J above. Let $N_x = N_y = 51$ and $N_z = 21$ be the number of discrete points in x; y and z directions, respectively. Therefore, the same grid step size h = 0:2 in these directions is used. For each i = 1; N, we denote by $v_i(x_i; y_j; z_l)$ the corresponding discrete function of $v_i(x; y; z)$ dened at mesh-points $x_i = R + ih; y_j = R + jh; z_l = b + lh$. Hereby, the corresponding Laplace operator in this nite dierence setting is given by = @ h + @ h + @ h, where, for interior grid points xx yy z bf, we consider

and the same is applied to the dierence operators $@_{yy}^h, @_{zz}^h$. For the gradient operator, we consider $r^h = (@_x^h; @_y^h; @_z^h)$ with

$$Q^h v_i(x_i; y_j; z_i) = (2h)^{-1} (v_i(x_{i+1}; y_j; z_i) v_i(x_{i-1}; y_j; z_i))$$
:

Henceforth, the discrete version of J corresponding to (30) is given by

$$\begin{split} J\left(V^{h}\right) &= h^{3} \sum_{j=1}^{X_{l}} \sum_{l=1}^{X_{l}} \sum_{i=1}^{N} \sum_{i=1}^{N} v_{i}(x_{i};y_{j};z_{l}) = 1 \\ &+ \sum_{i;j=1}^{X^{N}} P_{lij} r^{h} v_{i}(x_{i};y_{j};z_{l}) r^{h} v_{j}(x_{i};y_{j};z_{l}) + \sum_{i=1}^{X^{N}} Q_{li}(x_{i};y_{j};z_{l}) r^{h} v_{i}(x_{i};y_{j};z_{l}) \\ &+ \|h^{3} \sum_{j=1}^{X_{l}} \sum_{l=1}^{N} \sum_{l=1}^{N} \left(X_{i};y_{j};z_{l}\right) j^{2} + j r^{h} v_{l}(x_{i};y_{j};z_{l}) j^{2} + j^{h} v_{l}(x_{i};y_{j};z_{l}) j^{2} \right) \end{split}$$

To speed up the computation process, we compute the gradient DJ of the discrete functional J in (31) using the technique of Kronecker deltas; see in [23]. For brevity, we do not provide such a long formulation for the gradient DJ here. Overall, the procedure to compute the approximate minimizer, denoted by V comp, is described in Algorithm 1. For the step size in Algorithm 1, we briev report that we start from = 10 1, and for each iterative step, if the value of the functional exceeds its value on the previous step, we replace the current step size by =2. Otherwise, we keep it the same. We stop the minimization process via the gradient descent method when = 10^{-9} .

Algorithm 1 A numerical method to solve (27)

- 1: Choose a threshold error " > 0.
- 2: Set m = 0 and nd an initial solution V_0 by solving (28).
- 3: Compute V_{m+1} using the gradient descent method for some step size 0 < 1.
- 4: If $kV_{m+1} = V_m k_{[H^2]} = V_m k_{[M^2]} = V_m k_{[M^2$

After obtaining the computed N-dimensional vector function V comp, we plug its components in the Fourier series that approximates v. Then, we compute the unknown dielectric constant by the following discrete formulation:

$$c^{h}(x_{i}; y_{j}; z_{l}) = mean_{k} Re^{-h}v(x_{i}; y_{j}; z_{l}; k) + k^{2}(r^{h}v(x_{i}; y_{j}; z_{l}; k))^{2} + \frac{2r^{h}v(x_{i}; y; z_{l}; k) r^{h}u_{0}(x_{i}; y_{j}; z_{l}; k)}{\frac{1}{y}u(x_{i}; y_{j}; z_{l}; k)} + 1:o$$

To visually represent the reconstructed inclusion in each example, we use the isovalue function in MATLAB to generate 3D images. In cases where the inclusion possesses a high dielectric constant (10), we choose an isovalue of 20%. Conversely, for inclusions with low dielectric constants (< 10), we select an isovalue of 10%.

Numerical results

Our numerical results are depicted in Figures 48 corresponding to ve (5) examples that we have men-tioned earlier in subsection 4.4.1. In those gures, we present real photos of the experimental objects, and the reconstructed inclusions in three dimensions from two dierent computational approaches for comparison. Herewith, the rst one is our current approach when using multi-frequency data and a xed point source. The second approach is the one investigated in a series of publications [1315] dealing with the context of multiple point sources and a xed frequency.

In all gures, we nd that the rst method reconstructs our inclusions with better shapes. Specically, at this time the whole complicated shape of letters 'U', 'A' and 'O' is visible when applying the rst approach; see Figures 6, 7 and 8. Also, in Figure 5(b), the bottle of water with its cap can be well interpreted, compared to Figure 5(c) in which the second approach is used. We, however, observe numerically that there is a main drawback of the current numerical approach. Our approach in this context (i.e. multiple frequencies and one source) does not give a decent value of dielectric constant. For instance, in the rst test with the metallic cylinder, we report that the maximum value of the computed dielectric constant is only 1.0006, while by the second approach (i.e. multiple sources and one frequency), the obtained value is 18.72.

Example	1	2	3	4	5
Object	Metallic cylinder	Bottle of water	Wood U N	letallic A Me	tallic O
C ^h	18.72	23.29	6.56	15.01	16.25
Ctrue	10 - 29	23.8	2 - 6	10 - 29	10 - 29
Reference	[22]	[30]	[1]	[22]	[22]

TABLE 3. Values of computed and true dielectric constants of examples 15. The values are taken from [13].

Note that we, herewith, focus on the so-called appearing dielectric constant of metallic objects we have experimented numerically with in the previous publication [22]. In particular, the range of the appearing dielectric constant of metals is [10, 30].

As one of important physical properties that one targets in landmine detection, shape of reconstructed inclusion is essential and can be helpful in classifying explosive devices in the battleeld. Our reconstruction results show that the perspective of multiple frequencies and one source being considered in this work does a good job to full this property. It, indeed, produces a quite good shape of buried objects. With the same experimentally collected data used but dierent perspective (multiple sources and one frequency), the convexication method therein provides a high accuracy of computing the dielectric constant; see Table 2 in [13]. Note that having an accurate dielectric constant of the buried object is another essential physical property in landmine detection. Henceforth, when data set is allowed, it is our idea that one should combine these two perspectives to obtain decent reconstruction results in terms of both shape of the buried object and the dielectric constant. In the future work, we will not an appropriate approximate model for this interesting idea. In other words, a convexication method should be studied to come up with the perspective of multiple sources and frequencies.

5. SUMMARY

In this paper, we have examined the numerical performance of our convexication method applied to a 3D coecient inverse problem using experimental data. Our study focuses on imaging buried objects within a sandbox, simulating the detection of landmines on a battleeld.

Previously, we employed the convexication method with a setup involving multiple sources and a xed frequency. This approach yielded highly accurate computations of the dielectric constants. Meanwhile, we observed that using multiple frequencies and a xed source conguration improved the shape of the front surface of the experimental inclusions, a crucial physical property for detecting explosive devices.

Based on our current investigation, it is evident that combining these two congurations produces good reconstruction results in terms of both the shape of the buried object and the dielectric constant, provided the data set allows for such combination.

ACKNOWLEDGMENTS

V. A. Khoa thanks Dr. Darin Ragozzine (Brigham Young University, USA) for the recent support of his research career. V. A. Khoa was supported by NSF grant #DMS-2316603. L. H. Nguyen was supported by NSF Grant #DMS-2208159.

REFERENCES

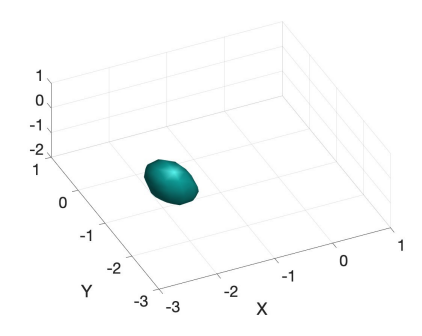
^{1.} Clipper Controls Inc. 2020 Dielectric Constants of Various Materials. http://clippercontrols.com/pages/Dielectric-Constant-Values.html#W.

^{2.} A. D. Agaltsov, T. Hohage, and R. G. Novikov. An iterative approach to monochromatic phaseless inverse scattering. Inverse Problems, 35(2):024001, 2018.

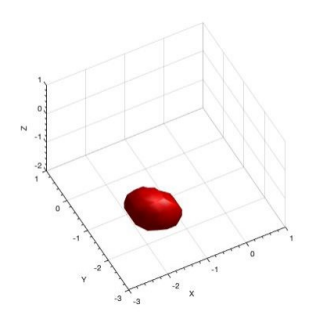
^{3.} N. V. Alekseenko, V. A. Burov, and O. D. Rumyantseva. Solution of the three-dimensional acoustic inverse scattering problem. The modied Novikov algorithm. Acoustical Physics, 54(3):407419, may 2008.



(a) Metallic cylinder



(b) The reconstructed metallic cylinder with one source and multiple frequencies



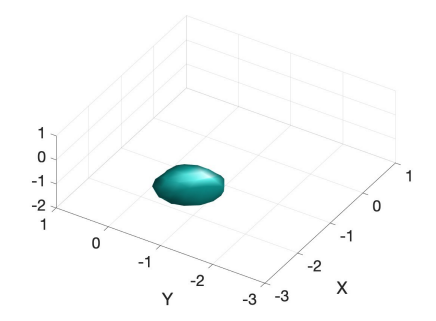
(c) The reconstructed of a metallic cylinder with multiple sources and a xed frequency

FIG. 4. Example 1. Metallic cylinder. (a) Real photo of aluminum cylinder. (b) The reconstructed dielectric constant function by the rst method with a xed source and multiple frequencies. (c) The reconstructed dielectric constant function by the second method with multiple sources and a xed frequency.

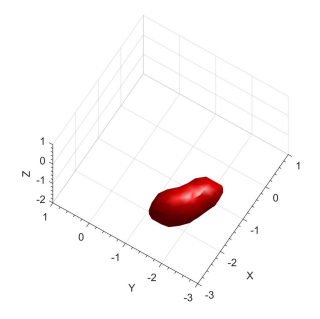
- 4. A. B. Bakushinskii and A. S. Leonov. Numerical solution of an inverse multifrequency problem in scalar acoustics. Computational Mathematics and Mathematical Physics, 60(6):987999, jun 2020.
- 5. E. Banks. Anti-Personnel Landmines: Recognising & Disarming. Brassey's Essential Guides, 1997.
- 6. L. Beilina and M. V. Klibanov. Approximate Global Convergence and Adaptivity for Coecient Inverse Problems. Springer US, 2012.
- 7. A. L. Bukhgeim and M. V. Klibanov. Global uniqueness of aclass of multidimensional inverse problems. Doklady Akademii Nauk SSSR, 260(2):269272, 1981. English translation: Soviet Mathematics Doklady, 24(2) (1981), 244247.
- 8. G. Chavent. Nonlinear Least Squares for Inverse Problems. Springer Science+Business Media B.V., 2010.
- 9. D. Colton and R. Kress. Inverse Acoustic and Electromagnetic Scattering Theory. Springer Berlin Heidelberg, 1992.
- 10. D. J. Daniels. A review of GPR for landmine detection. Sensing and Imaging: An International Journal, 7(3):90123, 2006.
- 11. A. V. Goncharsky and S. Y. Romanov. A method of solving the coecient inverse problems of wave tomography. Computers & Mathematics with Applications, 77(4):967980, 2019.
- 12. A. V. Goncharsky, S. Y. Romanov, and S. Y. Seryozhnikov. Low-frequency ultrasonic tomography: Mathematical methods and experimental results. Moscow University Physics Bulletin, 74(1):4351, 2019.
- 13. V. A. Khoa, G. W. Bidney, M. V. Klibanov, L. H. Nguyen, L. H. Nguyen, A. J. Sullivan, and V. N. Astratov.



(a) Bottle of water



(b) The reconstructed bottle of water with one source and multiple frequencies



(c) The reconstructed bottle of water with multiple sources and a xed frequency

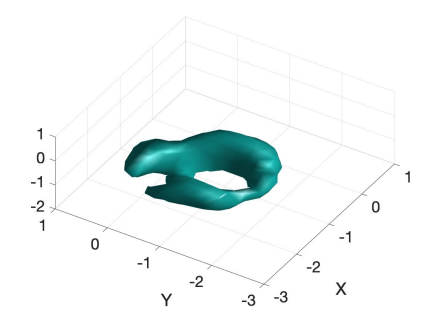
FIG. 5. Example 2. The bottle of water. (a) The real image of the glass bottle of water. (b) The reconstructed dielectric constant function by the rst method with a xed source and multiple frequencies. (c) The reconstructed dielectric constant function by the second method with multiple sources and a xed frequency. Clearly, we successfully detected the shape of the bottle of water by these two methods.

Convexication and experimental data for a 3D inverse scattering problem with the moving point source. Inverse Problems, 36(8):085007, 2020.

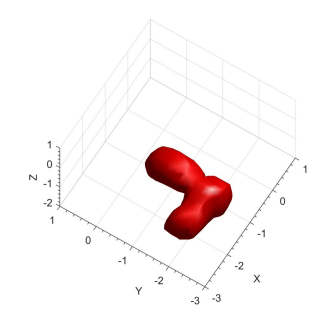
- 14. V. A. Khoa, G. W. Bidney, M. V. Klibanov, L. H. Nguyen, L. H. Nguyen, A. J. Sullivan, and V. N. Astratov. An inverse problem of a simultaneous reconstruction of the dielectric constant and conductivity from experimental backscattering data. Inverse Problems in Science and Engineering, 29(5):712735, 2020.
- 15. V. A. Khoa, M. V. Klibanov, and L. H. Nguyen. Convexication for a three-dimensional inverse scattering problem with the moving point source. SIAM Journal on Imaging Sciences, 13(2):871904, 2020.
- 16. M. V. Klibanov. Carleman estimates for global uniqueness, stability and numerical methods for coecient inverse problems. Journal of Inverse and III-Posed Problems, 21(4), 2013.
- 17. M. V. Klibanov. Convexication of restricted Dirichlet-to-Neumann map. Journal of Inverse and III-posed Problems, 25(5), 2017.
- 18. M. V. Klibanov, V. A. Khoa, A. V. Smirnov, L. H. Nguyen, G. W. Bidney, L. H. Nguyen, A. J. Sullivan, and V. N. Astratov. Convexication inversion method for nonlinear SAR imaging with experimentally collected data. Journal of Applied and Industrial Mathematics, 15(3):413436, 2021.
- 19. M. V. Klibanov, A. E. Kolesov, A. Sullivan, and L. Nguyen. A new version of the convexication method for a



(a) Wooden letter 'U'



(b) The reconstructed letter 'U' with one source and multiple frequencies



(c) The reconstructed letter 'U' with multiple sources and a xed frequency

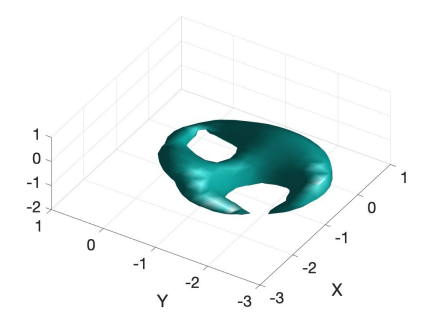
FIG. 6. Example 3. The wooden letter 'U'. (a) The real image of the U-shaped piece of dry wood. (b) The reconstructed dielectric constant function by the rst method with a xed source and multiple frequencies. (c) The reconstructed dielectric constant function by the second method with multiple sources and a xed frequency. Note that the U shape can be seen clearly by the rst method. It is well known that detecting non-convex objects with voids inside them is challenging but the rst method can produce clearly letter U and the void inside it.

1D coecient inverse problem with experimental data. Inverse Problems, 34(11):115014, 2018.

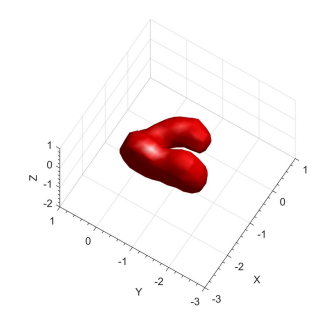
- 20. M. V. Klibanov and J. Li. Inverse Problems and Carleman Estimates Global Uniqueness, Global Convergence and Experimental Data. de Gruyter GmbH, Walter, 2021.
- 21. M. V. Klibanov, J. Li, and W. Zhang. Numerical solution of the 3-D travel time tomography problem. Journal of Computational Physics, 476:111910, 2023.
- 22. A. V. Kuzhuget, L. Beilina, M. V. Klibanov, A. Sullivan, L. Nguyen, and M. A. Fiddy. Blind backscattering experimental data collected in the eld and an approximately globally convergent inverse algorithm. Inverse Problems, 28(9):095007, 2012.
- 23. A. V. Kuzhuget and M. V. Klibanov. Global convergence for a 1-D inverse problem with application to imaging of land mines. Applicable Analysis, 89(1):125157, 2010.
- 24. T. T. Le and L. H. Nguyen. The gradient descent method for the convexication to solve boundary value problems of quasi-linear PDEs and a coecient inverse problem. Journal of Scientic Computing, 91(3), 2022.
- 25. T. T. T. Le and L. H. Nguyen. A convergent numerical method to recover the initial condition of nonlinear parabolic equations from lateral Cauchy data. Journal of Inverse and III-posed Problems, 30(2):265286, 2020.
- 26. D.-L. Nguyen, M. V. Klibanov, L. H. Nguyen, and M. A. Fiddy. Imaging of buried objects from multi-frequency experimental data using a globally convergent inversion method. Journal of Inverse and III-posed Problems, 26(4):501522, 2017.



(a) Metallic letter 'A'



(b) The reconstructed letter 'A' with one source and multiple frequencies



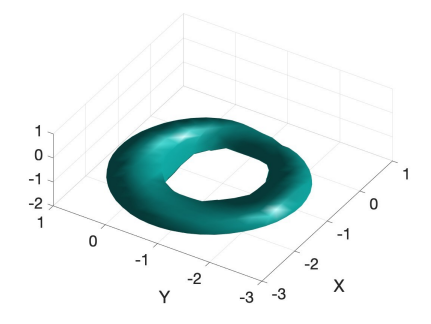
(c) The reconstructed letter 'A' with multiple sources and a xed frequency

FIG. 7. Example 4. The metallic letter 'A'. (a) The real image of the A-shaped piece of metal. (b) The reconstructed dielectric constant function by the rst method with a xed source and multiple frequencies. (c) The reconstructed dielectric constant function by the second method with multiple sources and a xed frequency. Note that letter A is produced perfectly with the void inside by the rst method. It is much clearer than the result obtain by the second method.

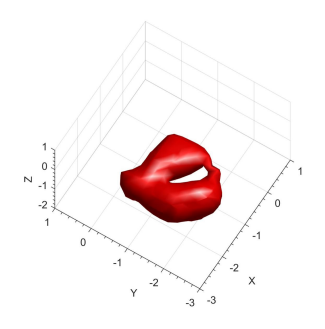
- 27. R. G. Novikov. An iterative approach to non-overdetermined inverse scattering at xed energy. Sbornik: Mathematics, 206(1):120134, jan 2015.
- 28. Oce of the Chief of Ordnance. Catalog of enemy ordnance materiel. In World War II Operational Documents, number N2228-E. http://cgsc.contentdm.oclc.org/cdm/ref/collection/p4013coll8/id/2758, 1945.
- 29. B. T. Polyak. Introduction to optimization. Optimization Software, Publications Division, 1987.
- 30. Nguyen Trung Thành, Larisa Beilina, Michael V. Klibanov, and Michael A. Fiddy. Imaging of buried objects from experimental backscattering time-dependent measurements using a globally convergent inverse algorithm. SIAM Journal on Imaging Sciences, 8(1):757786, 2015.



(a) Metallic letter 'O'



(b) The reconstructed letter 'O' with one source and multiple frequencies



(c) The reconstructed letter 'O' with multiple sources and a xed frequency

FIG. 8. Example 5. The metallic letter 'O'. (a) The real image of the O-shaped piece of metal. (b) The reconstructed dielectric constant function by the rst method with a xed source and multiple frequencies. (c) The reconstructed dielectric constant function by the second method with multiple sources and a xed frequency. It is clear that the O shape with a void inside is produced better by the rst method in comparison with the result of the second one.